

# Predicting brain tumour enhancement from non-contrast MR imaging with artificial intelligence

---

James K. Ruffle<sup>1,2,\*</sup>, Samia Mohinta<sup>1</sup>, Guilherme Pombo<sup>3</sup>, Asthik Biswas<sup>4,†</sup>, Alan Campbell<sup>5,†</sup>, Indran Davagnanam<sup>2,†</sup>, David Doig<sup>2,†</sup>, Ahmed Hammam<sup>2,†</sup>, Harpreet Hyare<sup>1,2,6,†</sup>, Farrah Jabeen<sup>2,7,†</sup>, Emma Lim<sup>8,9,†</sup>, Dermot Mallon<sup>1,2,†</sup>, Stephanie Owen<sup>2,†</sup>, Sophie Wilkinson<sup>6,†</sup>, Sebastian Brandner<sup>1,10</sup>, Parashkev Nachev<sup>1</sup>

<sup>1</sup>Queen Square Institute of Neurology, University College London, London, UK

<sup>2</sup>Lysholm Department of Neuroradiology, National Hospital for Neurology and Neurosurgery, London, UK

<sup>3</sup>NVIDIA, UK.

<sup>4</sup>Great Ormond Street Hospital for Children, London, UK.

<sup>5</sup>Imaging Department, Royal National Orthopaedic Hospital, Stanmore, Middlesex, UK

<sup>6</sup>Department of Radiology, University College Hospitals NHS Foundation Trust, London, UK.

<sup>7</sup>Department of Radiology, Royal Free Hospital, London, UK.

<sup>8</sup>Department of Imaging, Imperial College Healthcare NHS Trust, London, UK

<sup>9</sup>Department of Brain Sciences, Imperial College London, London, UK

<sup>10</sup>Division of Neuropathology and Department of Neurodegenerative Disease, Queen Square Institute of Neurology, University College London, London, UK

\*Correspondence to:

Dr James K Ruffle

Email: [j.ruffle@ucl.ac.uk](mailto:j.ruffle@ucl.ac.uk)

Address: Institute of Neurology, UCL, London WC1N 3BG, UK

†These authors contributed equally.

## **Funding**

JKR was supported by the Seed Grant funding programme of the European Society of Radiology (ESR) in collaboration with the European Institute for Biomedical Imaging Research (EIBIR) for undertaking this project. JKR is also supported by the Medical Research Council (MR/X00046X/1) and the British Society of Neuroradiology. HH and JKR are supported by the National Brain Appeal. PN is supported by the Wellcome Trust (213038/Z/18/Z). The UCLH NIHR Biomedical Research Centre supports JKR, HH, and PN.

## **Conflict of interest**

None to declare.

## **Manuscript Type**

Original article

## **Authorship**

JKR – led the study, design, data acquisition, analysis, manuscript drafting. SM, GP – data acquisition and analysis. AB, AC, ID, DD, AH, HH, FJ, EL, DM, SO, SW – radiology reviews, SB – data acquisition, PN – infrastructural support, analysis, manuscript drafting.

All authors have been involved in the writing of the manuscript and have read and approved the final version.

## **Keywords**

Brain tumours, deep learning, artificial intelligence, segmentation, gadolinium, contrast agent, magnetic resonance imaging.

## **Abbreviations**

AUROC, area under the receiver operator characteristic curve; BA, balanced accuracy; FLAIR, fluid attenuated inversion recovery; MRI, magnetic resonance imaging; NHNN, National Hospital for Neurology and Neurosurgery; SD, standard deviation.

## Abstract

---

Brain tumour imaging assessment typically requires both pre- and post-contrast MRI, but gadolinium administration is not always desirable, such as in frequent follow-up, renal impairment, allergy, or paediatric patients. We aimed to develop and validate a deep learning model capable of predicting brain tumour contrast enhancement from non-contrast MRI sequences alone. We assembled 11089 brain MRI studies from 10 international datasets spanning adult and paediatric populations with various neuro-oncological states, including glioma, meningioma, metastases, and post-resection appearances. Deep learning models (nnU-Net, SegResNet, SwinUNETR) were trained to predict and segment enhancing tumour using only non-contrast T1-, T2-, and T2/FLAIR-weighted images. Performance was evaluated on 1109 held-out test patients using patient-level detection metrics and voxel-level segmentation accuracy. Model predictions were compared against 11 expert radiologists who each reviewed 100 randomly selected patients. The best-performing nnU-Net achieved 83% balanced accuracy, 91.5% sensitivity, and 74.4% specificity in detecting enhancing tumour. Enhancement volume predictions strongly correlated with ground truth ( $R^2=0.859$ ). The model outperformed expert radiologists, who achieved 69.8% accuracy, 75.9% sensitivity, and 64.7% specificity. 76.8% of test patients had Dice  $\geq 0.3$  (acceptable detection), 67.5% had Dice  $\geq 0.5$  (good detection), and 50.2% had Dice  $\geq 0.7$  (excellent detection). Deep learning can identify contrast-enhancing brain tumours from non-contrast MRI with clinically relevant performance. These models show promise as screening tools and may reduce gadolinium dependence in neuro-oncology imaging. Future work should evaluate clinical utility alongside radiology experts.

## Introduction

---

Imaging diagnosis and surveillance play a key role in neuro-oncological care across both adult and paediatric populations<sup>1,2</sup>. The presence or absence of contrast enhancement is often critical to clinical decision-making. Contrast agents, however, cannot always be given, owing to contraindications such as allergies or renal impairment, or patient refusal. Imaging may also be corrupted by artefacts, making its radiological interpretation difficult. Furthermore, it is judged desirable to minimise repeated gadolinium use, especially in paediatric patients, though the risk of inadequate characterisation of the tumour is typically perceived to outweigh the risk of repeated gadolinium administration. Known risks aside, such as the development of nephrogenic systemic fibrosis<sup>3</sup>, the long-term effects of gadolinium exposure and its bodily deposition remain unknown<sup>4</sup>.

Beyond the individual patient, the widespread use of gadolinium contrast agents in medical imaging has a broader environmental impact. Although only small amounts are used in each study, the cumulative impact at a global scale results in substantial amounts (in the order of many thousands of litres) of gadolinium administered, secreted and/or disposed of each year<sup>5</sup>. Gadolinium has been detected in sewage, surface, drinking water<sup>6-8</sup>, water sources distant from MRI facilities<sup>9</sup>, and even in fast-food soft drinks<sup>10</sup>. Given uncertainty about the long-term impact of exposure, even at low doses, the problem has stimulated worldwide research efforts to reduce, or even eliminate, its use.

One possible solution to reducing contrast dependence is to use artificial intelligence to predict the presence of enhancement from non-contrast imaging alone. We have recently shown proof of concept that deep learning models can segment enhancing tumour tissue in glioma without contrast-enhanced imaging<sup>11</sup>. Similar works have also been investigated by others, both within the brain and other body parts, to either reduce gadolinium dosage<sup>12-14</sup> or eliminate it entirely in either lesion detection or image reconstruction<sup>13,15-17</sup>. Taken together, there is strong support that complex models can potentially leverage non-contrast MRI sequence information to derive post-contrast information from non-contrast scans.

Here, we prototype an enhanced intracranial disease prediction system using only non-contrast MRI data in the largest neuro-oncology imaging cohort known, combining state-of-the-art deep learning with large-scale unselective neuro-oncology data. Beyond scale, our methodological contributions include: (1) systematic comparison of CNN and transformer-based architectures; (2) uncertainty quantification to guide clinical deployment; (3) comprehensive equity calibration across demographic and clinical subgroups; and (4) direct benchmarking against expert human performance. Our findings strongly support the notion that complex models can learn features of what has historically been referred to as ‘enhancing’ disease, except with only non-contrast imaging sequences.

## Materials and Methods

---

### Data

We combined in-house and international open source brain tumour data to study a final patient population of 11089 unique patients diagnosed with a brain tumour (Figure 1). This cohort was as maximally heterogeneous and inclusive as could be achieved, spanning both adult and

paediatric patients, pre- and post-operative imaging, multiple neuro-oncological pathologies, and numerous global study sites (supplementary material). Imaging was acquired across multiple field strengths (1.5T and 3T) and MRI manufacturers between 2006 and 2024.

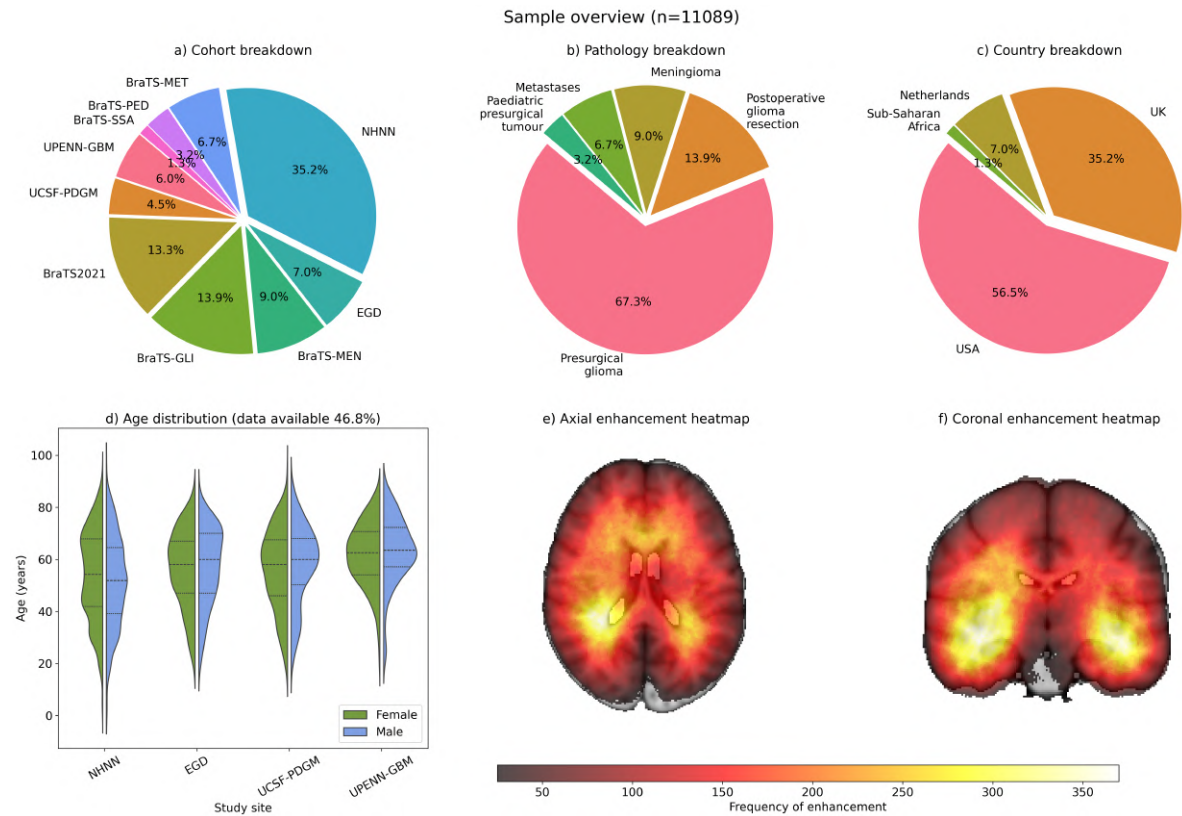


**Figure 1. Sample overview.** a) Cohort breakdown across the ten different study sites. b) Pathology type breakdown. c) Country of sample origin breakdown. d) Cohort age and sex distribution, where this data was available. e-f) Axial and coronal enhancing lesion distribution map with warmer colours indicating higher frequency of enhancement occurrence within a given location.

## Model development

We trained a series of deep learning models to segment enhancing tumours from non-contrast imaging sequences (Figure 2). Models were provided with the ground-truth labels of background (i.e., non-brain), normal brain parenchyma, non-enhancing abnormal tissue, and enhancing neuro-oncological disease, the latter being the primary target of interest. The enhanced tumour ground truth was derived from complete datasets, i.e. including post-contrast T1 sequences. All sequences within each imaging session were acquired during the same scanning session, pre-processed using gold standard approaches, and co-registered MNI space (supplementary material). Cases with substantial inter-sequence motion or registration failure on visual quality control were excluded. For postoperative cases, surgically related enhancement was distinguished from tumour enhancement by expert neuroradiological consensus within the source datasets. The model input, however, consisted only of non-contrast sequences, specifically T1-, T2-, and T2/FLAIR-weighted MRI sequences. We performed a randomised train-test split with 90% of the data allocated for training and 10% for model testing, ensuring no leakage between sets. This partition was fixed

for all model training runs to ensure maximal comparability. Validation was undertaken within the training set, and the test set was locked until all model development was complete.

Model architectures trained included nnU-Net (v2<sup>18,19</sup>, SegResNet<sup>20</sup>, and SwinUNET<sup>21,22</sup>. For nnU-Net, we trained the default 1000-epoch model and a 4000-epoch model with the large residual connection encoder modification, which represents a reasonable balance between computational cost and performance gain<sup>23</sup>. For SegResNet<sup>20</sup>, architectural parameters included 16 output channels for the initial convolution layer, a dropout probability of 0.1, and ReLU activation. For SwinUNETR<sup>21,22</sup>, architectural parameters included a feature size of 48, a dropout and attention dropout rate of 0.1. We used a learning rate of 0.001, the Adam optimizer, a cosine annealing learning scheduler, and Dice loss. For both SegResNet and SwinUNETR, we enabled a variety of augmentations, including foreground cropping and signal normalisation, random axis flipping, coarse dropout, intensity shift and scaling, bias field, histogram shifts, Gaussian smoothing, low resolution simulation, affine and 3D elastic deformations<sup>24</sup>. Data augmentations were enabled within nnU-Net per its creators' standard settings<sup>18,19</sup>. SegResNet and SwinUNETR models were trained for up to 4000 epochs, but with early stopping patience of 100 epochs. Hyperparameters were only tuned within the training set with internal validation of this set. Model training was undertaken on a Linux GPU-enabled (NVIDIA RTX 6000 Ada Generation) workstation. Training times were approximately 2000 hours (~83 days) per model.

## Evaluation

### Performance metrics

We evaluated the performance of trained segmentation models on a held-out test set. Model performance was assessed using both voxel-level and patient-level metrics. Voxel-wise metrics, i.e., the number of correctly classified pathologically enhancing and non-enhancing voxels within a given image, included the Dice coefficient, balanced accuracy, precision, recall, and F1 score. Bootstrapped (1000 iterations) patient-wise metrics were also derived for the overall classification of whether a study contained any pathologically enhancing tissue, quantified by balanced accuracy, precision, recall, and F1 score. For clinical interpretability, we defined detection success thresholds as follows: Dice  $\geq 0.3$  ('acceptable detection'); Dice  $\geq 0.5$  ('good detection'); and Dice  $\geq 0.7$  ('excellent detection'). Below Dice 0.3, predictions were considered clinically unreliable.

### Equity calibration

We quantified the epistemic equity of the model (i.e., fairness in model performance across different patient subgroups, ensuring equitable diagnostic utility regardless of patient characteristics)—variation in fidelity across patient attributes—as a function of its performance, considering the cohort site, the underlying pathology, the country of sample origin, the age and sex of the patient (where available)<sup>25,26</sup>, and the size and morphology (supplementary material).

## Comparison with radiologists

We subsequently conducted an assessment in which radiologists were tasked with predicting whether a lesion would enhance after contrast administration, using only the unenhanced images. To do this, 100 patients from the held-out test set were randomly allocated to each of the eleven individual experienced radiologists. The eleven radiologists comprised board-certified specialists (post-FRCR, post-CCT) with either formal neuroradiology subspecialty training or extensive neuro-oncological imaging experience (median years in practice: 11.3, IQR 7.5-14.5). All regularly reported brain tumour MRI as part of routine clinical practice across six large London-based hospitals. Cases were randomly sampled from the held-out test set, with each radiologist reviewing a unique, non-overlapping set of 100 cases (50 with enhancing abnormality, 50 without), yielding 1,100 total case-reader evaluations across 447 unique imaging sessions. Radiologists accessed anonymised imaging through ITKSnap on a Linux workstation with a 4K monitor. No time limit was imposed. Readers were informed that approximately half of the cases would contain enhancing lesions but were not provided with additional clinical context. Cases were presented in a randomised order to minimise recall bias. Imaging for fifty patients would contain an enhancing abnormality, and fifty did not. Each radiologist sequentially reviewed the unenhanced MRI images (T1-, T2-, and T2/FLAIR-weighted) from each case and was asked: “Do you think there will be an enhancing abnormality in this case?” We then statistically compared the model's predictions with those of the radiologist, with both sets related to the ground truth.

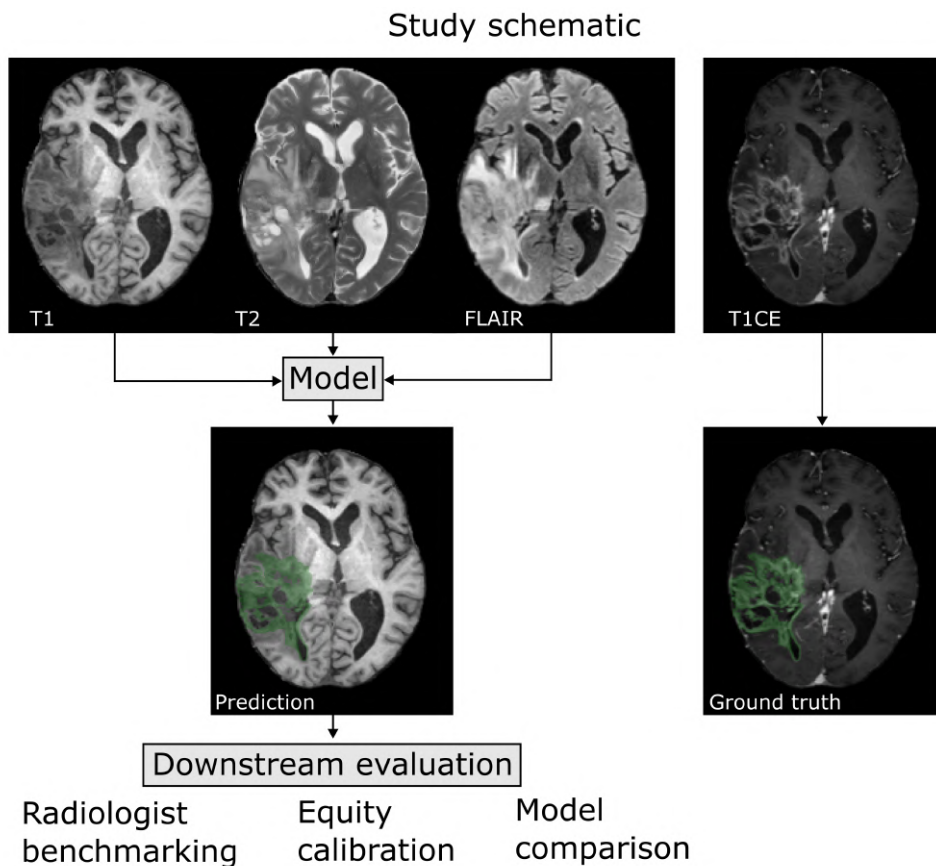


**Figure 2. Study schematic.** The model was trained to predict enhancing intracranial disease from T1-, T2-, and T2/FLAIR-weighted imaging alone. This was evaluated alongside a ground truth derived from all sequences, including the postcontrast T1 (T1CE). Downstream model evaluation was undertaken by conventional model comparison, radiologist benchmarking, and equity assessments.

## Analytic compliance

All analyses were performed and reported following TRIPOD and PROBAST-AI guidelines<sup>27</sup>. Classical statistical tests included logistic regression, one-way ANOVA, t-tests, and Levene's test for equality of variances. Statistical tests were corrected for multiple comparisons by Bonferroni with corrected p values reported accordingly.

## Code, model, and data availability

The software shall be openly available upon publication. Most of the patient data utilised in this article is freely and publicly available<sup>28-36</sup>. Our study ethics preclude the release of internal data. The following Python software and models were used for model development and downstream analyses: Fairboard, Matplotlib<sup>37</sup>, MONAI<sup>38</sup>, Nibabel<sup>39</sup>, Nilearn<sup>40</sup>, NumPy<sup>41</sup>, pandas<sup>42</sup>, PyTorch<sup>43</sup>, seaborn<sup>44</sup>, scikit-learn<sup>45</sup>, and TumourSeg<sup>11</sup>.

## Informed consent

The consent process for external datasets is described within the source publications<sup>28-31,33-36</sup>. The local ethics committee approved consentless use of irrevocably anonymised local data under standard opt-out frameworks.

## Ethics

The local ethics committee at University College London approved the study. We received ethical permission for the consentless analysis of local irrevocably anonymised data collected during routine clinical care. All external datasets were also granted ethical approval as described within the source datasets<sup>28-31,33-36</sup>.

## Results

---

### Cohort

The study cohort included 11089 imaging sessions, with 9980 allocated to the training dataset and 1109 assigned to model testing. Patient age was available for 5187 patients (46.78%), with a mean  $\pm$  standard deviation of  $55 \pm 16.44$  years. Patient sex was available for 5651 patients (50.96%), 3061 of whom were male, and 2590 were female. There were no significant differences in patient age ( $p=0.76$ ) and sex ( $p=0.38$ ) between the training and test datasets, nor was there a significant difference in site breakdown (all  $p>0.05$ ) (Supplementary Figure 1).

### Clinical performance in detecting enhancement on non-contrast MRI

The mean balanced accuracy at the sample level, i.e., the model's ability to detect whether a patient's imaging study contained an enhancing tumour, was  $0.830 \pm$  standard deviation (SD)  $0.150$ . The model's mean sensitivity (recall), specificity, precision, and F1 score were  $0.915 \pm 0.009$ ,  $0.744 \pm 0.041$ ,  $0.968 \pm 0.006$ , and  $0.941 \pm 0.006$ , respectively. Sample patients across all different imaging cohorts are shown below in Figure 3.

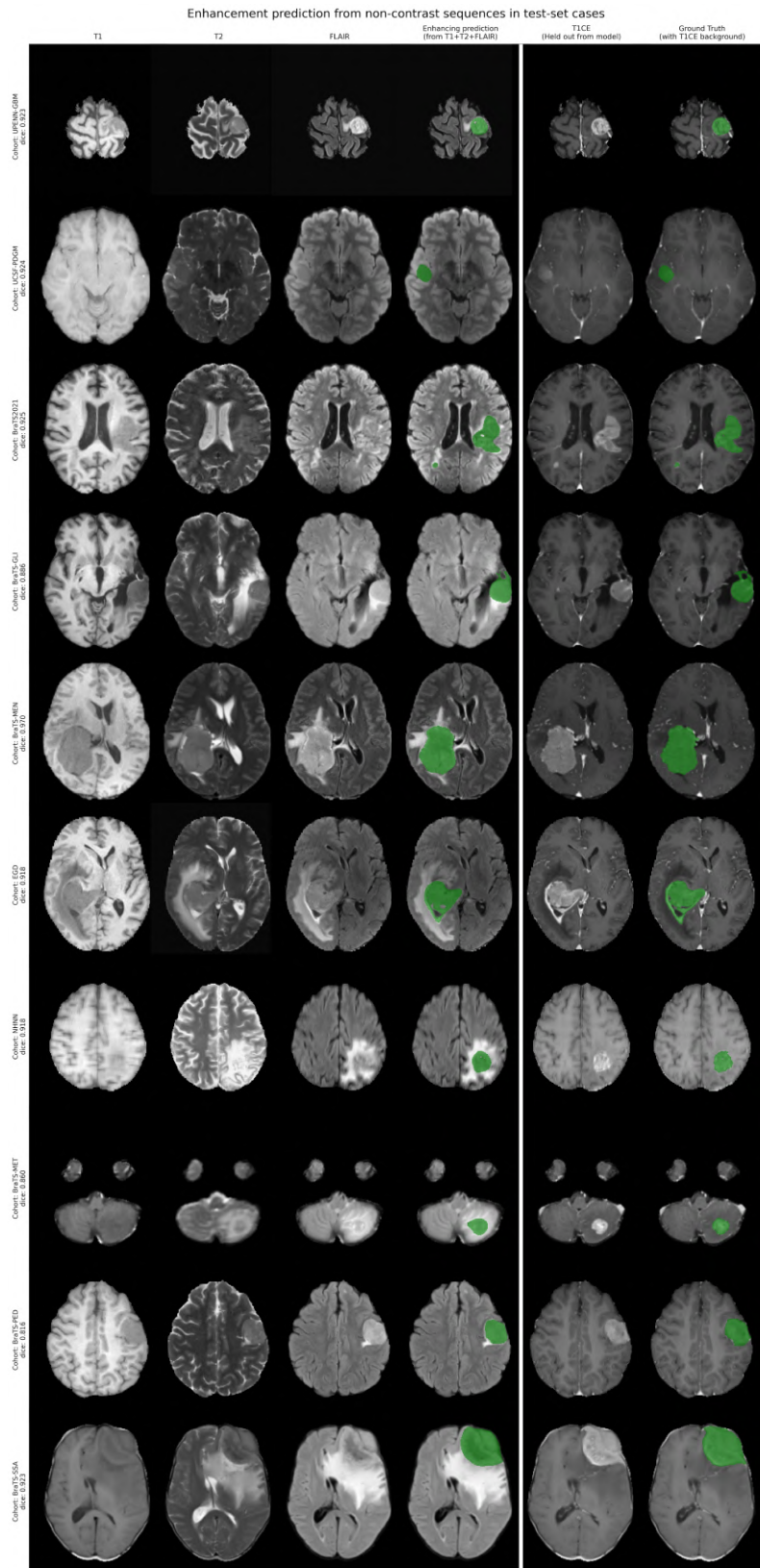


**Figure 3. Enhancement prediction from non-contrast sequences in test-set cases.** Representative test-set case from each cohort demonstrating the model's ability to predict contrast enhancement from non-contrast MRI sequences. Each row shows a different case with six columns: T1-weighted, T2-weighted, T2/FLAIR (Fluid-Attenuated Inversion Recovery), model prediction of enhancing tumour from the unenhanced T1, T2 and FLAIR images (green overlay on T2/FLAIR), T1CE (T1 contrast-enhanced, withheld during model training), and ground truth enhancing tumour segmentation (overlay on T1CE). Held-out T1CE images confirm that the model predictions align with actual contrast enhancement patterns.

## Comparison with expert radiologists

In comparison, the mean balanced accuracy of the radiologists' ability to detect whether a patient's imaging study contained an enhancing tumour was lower at  $0.698 \pm 0.072$ . The radiologists' mean sensitivity (recall), specificity, precision, and F1 score were  $0.759 \pm 0.076$ ,  $0.647 \pm 0.151$ ,  $0.680 \pm 0.091$ , and  $0.713 \pm 0.056$ , respectively. Across the expert radiologist trials, 100 of the 447 (22.4%) unique imaging sessions were wrongly labelled as they would not contain enhancing tumour. In comparison, 35 of 447 (7.8%) unique imaging sessions were wrongly labelled by the model as not containing enhancing tumour. For the 100 cases wrongly labelled by radiologists, 79 of them (79.0%) that were labelled not to contain enhancing tumour by radiologists were correctly labelled by the model. In contrast, 14 of 35 (40.0%) of unique imaging sessions that the model wrongly labelled as not containing enhancing tumour were correctly labelled by the radiologists. Sample patients wrongly reported by radiologists but correctly identified by the model are shown in Figure 4.

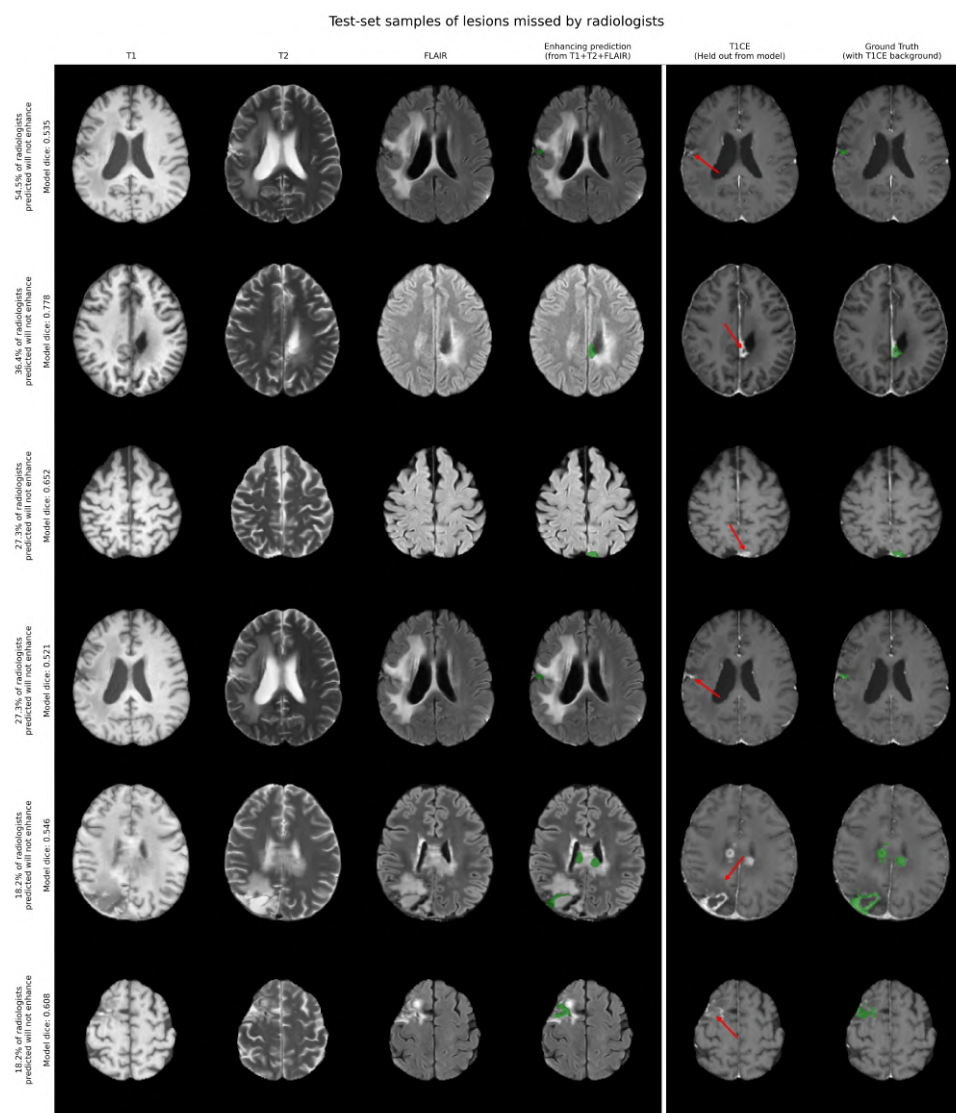


**Figure 4. Test-set samples of lesions missed by radiologists.** Representative test-set cases that radiologists wrongly predicted to contain no post-contrast enhancement when reviewing the non-contrast imaging. Each row shows a different case with six columns: T1-weighted, T2-weighted, FLAIR (Fluid-Attenuated Inversion Recovery), model prediction of enhancing tumour from the T1, T2 and FLAIR (green overlay on FLAIR), T1CE (T1 contrast-enhanced, withheld during model training), and ground truth enhancing tumour segmentation (overlay on T1CE). Held-out T1CE images confirm that the model predictions align with actual contrast enhancement patterns.

## Equity calibration

Enhanced detection performance was reasonably robust throughout the 1109 test-set across all datasets, pathologies, countries, patient ages, and sexes (balanced accuracy (BA)) range 0.739-1.000) (Figure 5). Slightly lower performances were observed in postoperative glioma resection cases (BA 0.825), paediatric presurgical tumours (BA 0.739), and within our internal NHNN cohort (BA 0.790). Detection performance was lower in individuals 30 years or younger (BA 0.609), but stronger for the remaining age groups (BA range 0.773-0.866). Detection performances were equivalent for men and women.

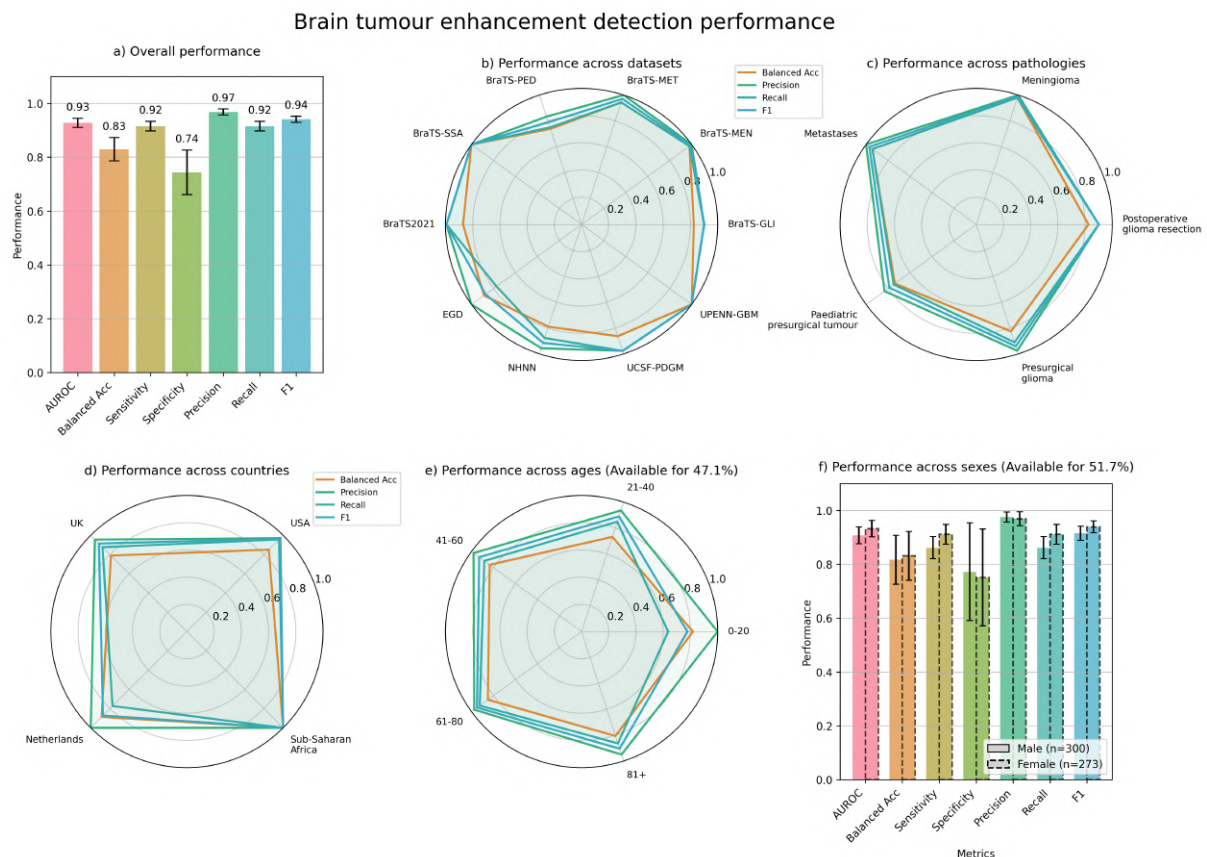


**Figure 5. Brain tumour enhancement detection performance.** Model performance in detecting enhancing tumour from non-contrast sequences (where Dice > 0.3). Performances across the a) entire cohort, datasets, pathologies, countries, e) ages and f) sex. Bars in panels a and f are shown with bootstrapped confidence intervals.

## Voxel-level segmentation performance

The best-performing MRI non-contrast segmentation model was the 4000-epoch trained nnU-Net with the large residual encoder, which achieved an out-of-sample segmentation performance by mean  $\pm$  SD Dice coefficient across the different components as follows: normal brain ( $0.987 \pm 0.024$ ), non-enhancing abnormal tissue ( $0.821 \pm 0.233$ ), and enhancing tumour ( $0.574 \pm 0.319$ ). Mean segmentation (voxel-wise) balanced accuracy across normal brain, non-enhancing abnormal tissue, and enhancing tumour was  $0.990 \pm 0.013$ ,  $0.992 \pm 0.098$ , and  $0.790 \pm 0.168$ , respectively. Mean precision across normal brain, non-enhancing abnormal tissue, and enhancing tumour components was  $0.992 \pm 0.028$ ,  $0.844 \pm 0.213$ , and  $0.686 \pm 0.284$ , respectively. Mean sensitivity (recall) across normal brain, non-enhancing

abnormal tissue, and enhancing tumour components was  $0.983 \pm 0.021$ ,  $0.846 \pm 0.197$ , and  $0.581 \pm 0.337$ , respectively. Mean F1 score across normal brain, non-enhancing abnormal tissue, and enhancing tumour components was  $0.987 \pm 0.024$ ,  $0.821 \pm 0.233$ , and  $0.557 \pm 0.329$ , respectively. Evaluating clinical performance thresholds, we observed that 76.8% of test-set cases had a Dice score of  $\geq 0.3$  (acceptable detection), 67.5% of cases had a Dice score of  $\geq 0.5$  (good detection), and 50.2% of cases had a Dice score of  $\geq 0.7$  (excellent detection).

For cases positive for enhancing tumour (992 of 1109 cases), cohort metrics were as follows: UPENN-GBM, Dice  $0.824 \pm 0.085$  (n=68, success rate [where Dice  $\geq 0.3$ ] 100.0%); BraTS-MEN, Dice  $0.809 \pm 0.239$  (n=100, success rate 93.0%); BraTS2021, Dice  $0.766 \pm 0.185$  (n=139, success rate 96.4%); BraTS-SSA, Dice  $0.717 \pm 0.151$  (n=16, success rate 100.0%); UCSF-PDGM, Dice  $0.704 \pm 0.304$  (n=43, success rate 83.7%); EGD, Dice  $0.533 \pm 0.334$  (n=75, success rate 73.3%); BraTS-MET, Dice  $0.510 \pm 0.291$  (n=70, success rate 74.3%); BraTS-GLI Dice  $0.496 \pm 0.283$  (n=111, success rate); NHNN Dice  $0.423 \pm 0.313$  (n=350, success Rate 62.0%); and BraTS-PED Dice  $0.277 \pm 0.321$  (n=20, 45.0%). Grouped pathology performances were as follows: meningioma, Dice  $0.809 \pm 0.239$  (n=100, success rate 93.0%); presurgical glioma, Dice  $0.568 \pm 0.319$  (n=691, success rate 76.1%); metastases, Dice  $0.510 \pm 0.291$  (n=70, success rate 74.3%); postoperative glioma resection, Dice  $0.496 \pm 0.283$  (n=111, success rate 73.9%); and paediatric presurgical tumour, Dice  $0.277 \pm 0.321$  (n=20, success rate 45.0%). The performances by country of dataset origin were as follows: Sub-Saharan Africa, Dice  $0.717 \pm 0.151$  (n=16, success rate 100.0%); USA, Dice  $0.672 \pm 0.284$  (n=551, success rate 86.0%); the Netherlands, Dice  $0.533 \pm 0.334$  (n=75, success rate 73.3%); and UK, Dice  $0.423 \pm 0.313$  (n=350, success rate 62.0%).

The burden of enhancing tumour was accurately predicted by the model with an  $R^2$  of 0.859 and a mean volumetric difference between the prediction and the ground truth of  $-1.30\text{cm}^3$  (Figure 6). There was a clear relationship between the case-level detectability of an enhancing lesion and its corresponding Dice score. Lesion detectability was more variable (with an approximate 50% success rate) for tiny lesions ( $\sim 0.01\text{cm}^3$ ) but correctly detected  $>90\%$  of the time when the lesions were  $2\text{cm}^3$  or larger.

As commonly reported in segmentation tasks, voxel-level performance did show some variation with lesion volume (ANOVA  $p < 0.0001$ ), as follows:  $< 0.5\text{cm}^3$  (n=140), mean Dice  $0.162 \pm \text{SD } 0.240$ ;  $0.5\text{-}1\text{cm}^3$  (n=58), mean Dice  $0.332 \pm 0.302$ ;  $1\text{-}5\text{cm}^3$  (n=170), mean Dice  $0.471 \pm 0.302$ ;  $5\text{-}10\text{cm}^3$  (n=126), mean Dice  $0.626 \pm 0.284$ ;  $> 10\text{cm}^3$  (n=498), mean Dice  $0.741 \pm 0.192$ . There was also some variation in segmentation performance related to radiomic characterisation of lesions (ANOVA  $p < 0.0001$ ) as follows: infiltrative lesions (n=473), mean Dice  $0.627 \pm 0.264$ ; irregular/complex lesions (n=326), mean Dice  $0.579 \pm 0.329$ ; multiple components (n=87), mean Dice  $0.459 \pm 0.321$ ; well circumscribed (n=82), mean Dice  $0.542 \pm 0.401$ . A lesion's detectability was significantly related to its size, expressed by the logistic regression  $y \sim 1.713 \log_{10}(V) - 4.786$ , where  $V$  denotes lesion volume,  $p < 0.0001$ , log-likelihood  $-361.464$ , Odds ratio per 10-fold increase in volume 5.546 (95% confidence interval 4.389-7.009). Model segmentation performance for a given pathology showed a trend for association with the number of available samples but did not reach statistical significance.

Relationship between model performance and lesion volume, morphology, and pathology

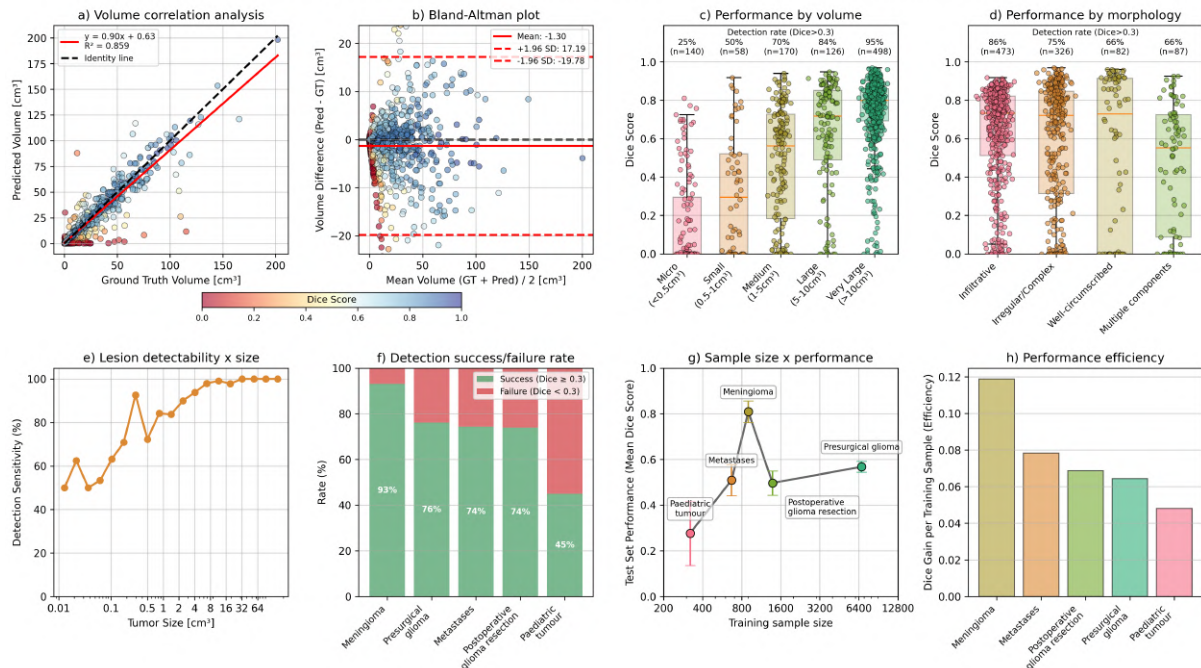


**Figure 6. Relationship between model performance and lesion volume, morphology, and pathology.** a) Volume correlation analysis showing strong agreement between predicted and ground truth enhancement. b) Bland-Altman plot assessing agreement between predicted and ground truth volumes, with mean difference (solid red line) and  $\pm 1.96$  standard deviation limits (red dashed lines). c) Segmentation performance (Dice coefficient) and successful detection rate (annotated percentage) stratified by volume categories. d) Detection rate by radiomics-derived morphological patterns. e) Lesion detection sensitivity as a function of enhancement size. f) Detection success (green) and failure (red) rates by pathology type. g) Relationship between training sample size and test set performance (Dice score) for each pathology type. h) Performance efficiency measured as Dice score gain per training sample, identifying pathologies with the highest learning efficiency.

## Outlier analysis

Examination of cases with poor segmentation performance (Dice < 0.3) revealed several contributing factors: (1) small lesion volume (< 0.5 cm<sup>3</sup>), accounting for the majority of failures; (2) postoperative cases with complex enhancement patterns including surgical cavity enhancement; (3) marked imaging artefact or suboptimal image quality in older acquisitions; and (4) atypical enhancement patterns, including faint, incomplete rim enhancement, or no enhancement to lesions that would ordinarily be expected to enhance (the latter particularly noted in paediatric cases). These observations suggest that model refinement should prioritise augmented training on challenging cases and potentially incorporate image quality assessment to flag unreliable predictions.

## Uncertainty estimation

We also assessed model probability maps (i.e. prior to the generation of the binary segmentation map). Across the 1109 test set, the mean probability within the enhancing tumour prediction channel was  $0.583 \pm 0.301$ , with a mean entropy of  $0.160 \pm 0.089$  (boundary fraction  $0.075 \pm 0.050$ ). There were 0 cases with high uncertainty (i.e. with entropy > 0.5). Assessment of model uncertainty with probability maps is shown further in the supplementary material (Supplementary Figure 2).

Disease-specific maximal predicted probabilities were as follows: presurgical glioma mean  $0.912 \pm \text{SD } 0.268$  ( $n=691$ ), postoperative glioma resection  $0.902 \pm 0.285$  ( $n=111$ ), meningioma  $0.976 \pm 0.123$  ( $n=100$ ), metastases  $0.944 \pm 0.224$  ( $n=70$ ), and paediatric presurgical tumour  $0.729 \pm 0.411$  ( $n=20$ ). Levene's test for equality of variances showed a significant difference ( $p=0.002$ ), demonstrating that model uncertainty was significantly more variable within the smaller pathology cohorts available. Sex-specific maximal predicted model probabilities were as follows: male  $0.871 \pm 0.316$  ( $n=274$ ), and female  $0.906 \pm 0.277$  ( $n=245$ ), where uncertainty variance did not significantly differ following multiple comparison correction. Age category maximal predicted model probabilities were as follows: 0-20 years  $0.636 \pm 0.481$  ( $n=11$ ), 21-40 years  $0.865 \pm 0.313$  ( $n=86$ ), 41-60 years  $0.892 \pm 0.294$  ( $n=180$ ), 61-80 years  $0.922 \pm 0.255$  ( $n=173$ ), and 81+ years  $0.870 \pm 0.324$  ( $n=22$ ), where variance did not significantly differ following multiple comparison correction.

## Discussion

---

We developed and evaluated a deep learning model for detecting and segmenting enhancing tumour from non-contrast magnetic resonance imaging sequences alone. In the largest known study of its kind, using large-scale international data across ten different cohorts, five different disease categories, and four countries, our findings provide strong support for the ability of complex models to identify and delineate enhancing intracranial disease from non-contrast MRI alone. Although detecting contrast-enhancing disease is widely held to require contrast administration, our finding that a model can predict enhancement with >83% accuracy from only non-enhanced images suggests otherwise. Sufficiently capable AI models may leverage information from pre-contrast imaging that human experts cannot perceive. Such models may pave the way for reducing the use of contrast agents.

We envision the predominant real-world utility of this model as a screening or triage tool rather than a complete replacement for contrast-enhanced imaging. In clinical practice, patients with high-confidence model predictions of no enhancement could potentially forgo contrast administration, particularly in settings where repeated imaging is required (e.g., surveillance follow-up), where contraindications exist (renal impairment, allergy), or where minimising gadolinium exposure is prioritised (paediatric patients). Conversely, patients with uncertain or positive predictions would proceed to standard contrast-enhanced imaging. This approach could significantly reduce gadolinium use while maintaining diagnostic safety.

Our model's performance, both as an enhancement detector and a segmentation tool, is competitive with the broader literature. Previous internal research has demonstrated a Dice segmentation performance of 0.79 in delineating enhancing tumour in the more homogeneous Brats 2021 glioma cohort from T1-, T2-, and T2/FLAIR-weighted imaging alone<sup>11</sup>. However, this was evaluated in a substantially smaller and more uniform sampling space. Here, we report Dice segmentation performance for gliomas (cohort-dependent) of up to 0.824 on the UPENN-GBM dataset, but observe more variable performance depending on lesional and imaging heterogeneity and the quality of the available imaging data. Specifically, our deliberate inclusion of internal 'real-world' clinical data (NHNN cohort), which dates back to 2006, demonstrates substantial differences in imaging quality across MRI manufacturers, field strengths, and other associated parameters. Other comparative studies include that of Kleesiek et al., who developed a Bayesian U-Net using T1-, T2-, T2/FLAIR-weighted,

diffusion-weighted imaging (b0, b1000, ADC), and susceptibility-weighted imaging (magnitude, phase, and minimum intensity projection) to produce virtual contrast maps in an 82-patient cohort<sup>46</sup>, reporting an AUROC of 0.847 for enhancing tumour detection in their 10-fold validation set (our model achieved an AUROC of 0.909 in an entirely held out test set, data not shown for validation set metrics). The inclusion of diffusion and susceptibility-weighted imaging by their group is particularly notable, not least because diffusion characteristics can assist radiologists to identify tumour hypercellularity<sup>47</sup>. Regarding methods of reducing gadolinium dose (but not eliminating it entirely, as done here), Ammari et al. reported an 83% sensitivity for lesions larger than 10mm using deep learning for virtual contrast prediction, employing a one-quarter gadolinium dose<sup>48</sup>, a task also undertaken by many others<sup>12,49</sup>. Murugesan et al. recently demonstrated similar feasibility in a single-institution glioma cohort<sup>50</sup>. Our study extends this approach to a substantially larger dataset (n=11,089) spanning multiple pathologies, age groups, and imaging protocols, thereby establishing broader generalisability.

Healthcare should be equitable, which extends to any such tool at our clinical disposal<sup>25,26</sup>. Artificial intelligence is one of the fields experiencing the fastest growth in research, industry, and society, with many purported applications across medicine<sup>51,52</sup>. Yet, the equity calibration of software to ensure it benefits everyone is rarely quantified. For these reasons, we assess the performance equity of our model as granularly as possible across the largest and most diverse available cohort. Our findings show that the model generally performs equitably regardless of patient age or sex, although it was less effective in paediatric populations. This weaker performance in paediatric cases is most likely partly due to our cohort containing substantially fewer paediatric cases than adults (only 3.17% paediatric, with the remainder adult). Although our sample is large in kind, paediatric patients were underrepresented compared to adults due to limited sample availability. Another potential, and likely combinatorial, factor is the inherent complexities of paediatric neuro-oncology, where enhancement patterns often vary significantly from those seen in adult lesions. Moreover, there is also considerable variability within the paediatric population itself, especially across the spectrum of paediatric low-grade gliomas and glioneuronal tumours. To our strength, the inclusion of maximally heterogeneous data from as many sources as was feasible will invariably maximise its generalizability, supported by other work highlighting the impact on model performance with distributional shift<sup>53-55</sup>, and routes such as federated learning or widened data sharing to overcome it<sup>54,56</sup>.

Our study has limitations. Firstly, the cohort disproportionately includes more adult than paediatric patients, and more larger than smaller lesions. Our research prioritised maximal inclusivity in all modelling tasks. To that end, the inclusion of *any* paediatric or small lesional samples (even if markedly imbalanced compared to the availability of adult cohort data) was deemed preferable to excluding the population from this analysis. Future work should include even larger cohorts with even more diverse caseloads to improve model performance in these subpopulations, whether through new model training or fine-tuning from model weights generated from adult data. To our strength, we tested this empirically within the analysis as a key part of model equitable calibration. We also included all data at our disposal, which encompassed global data from several countries and clinicodemographic populations, thereby providing greater generalizability than is often achieved in such studies. Secondly, though our model demonstrated a strong sensitivity (0.915) for detecting an enhancing lesion from unenhanced images, the specificity was not as strong (0.744) with more false positives than

false negatives. Future research could fine-tune these weights with additional data from further cohorts, including more non-enhancing tumours where available, given the imbalanced sample we had at our disposal. To our strength, one core purpose of such a model here would be to classify imaging sessions where lesions are highly likely to enhance, such that post-gadolinium imaging could be foregone for the initial scan, follow-up imaging or both. Therefore, a high sensitivity at the expense of specificity should be preferred. The practical implications of the model's specificity also warrant consideration. In a screening scenario where the model predicts enhancement that subsequently proves absent on contrast imaging, the consequence would be an 'unnecessary' contrast administration no different to current standard practice and thus incurs no additional patient risk beyond routine care. However, false-positive predictions could generate patient anxiety if communicated prior to confirmatory imaging and may complicate workflows if used to deterministically triage imaging protocols. We therefore would advocate that model predictions be integrated as clinical decision support tools rather than definitive pathway allocators.

In conclusion, we demonstrate that deep learning models can identify 'contrast-enhancing' intracranial disease in neuro-oncology when exposed to the non-contrast magnetic resonance imaging sequences alone. That a deep learning model can discern areas of pathological enhancement from non-enhanced images yields strong support for the advent of generative models in synthetically enhanced or low-dose enhanced post-contrast comparators<sup>49,57</sup>. In their current form, such approaches may be particularly valuable as screening or triage tools to minimise, rather than completely replace, contrast-enhanced imaging. However, we hope future increases in data availability, algorithmic complexity, and high-performance computing may offer further opportunities to innovate in this space. These findings may also advance understanding as to the radiological basis for lesional enhancement, radiological pedagogy<sup>58</sup>, and showcase the opportunities deep learning may bring for illuminating it as a means to reduce or even alleviate the need for contrast agents.

## References

- 1 Wen, P. Y. *et al.* RANO 2.0: Update to the Response Assessment in Neuro-Oncology Criteria for High- and Low-Grade Gliomas in Adults. *Journal of clinical oncology : official journal of the American Society of Clinical Oncology* **41**, 5187-5199 (2023). <https://doi.org/10.1200/JCO.23.01059>
- 2 Erker, C. *et al.* Response assessment in paediatric high-grade glioma: recommendations from the Response Assessment in Pediatric Neuro-Oncology (RAPNO) working group. *Lancet Oncol* **21**, e317-e329 (2020). [https://doi.org/10.1016/S1470-2045\(20\)30173-X](https://doi.org/10.1016/S1470-2045(20)30173-X)
- 3 Woolen, S. A. *et al.* Risk of Nephrogenic Systemic Fibrosis in Patients With Stage 4 or 5 Chronic Kidney Disease Receiving a Group II Gadolinium-Based Contrast Agent: A Systematic Review and Meta-analysis. *JAMA Internal Medicine* **180**, 223-230 (2020). <https://doi.org/10.1001/jamainternmed.2019.5284>
- 4 Anderson, M. A., Harrington, S. G., Kozak, B. M. & Gee, M. S. Strategies to Reduce the Use of Gadolinium-Based Contrast Agents for Abdominal MRI in Children. *AJR Am J Roentgenol* **214**, 1054-1064 (2020). <https://doi.org/10.2214/AJR.19.22232>
- 5 Dekker, H. M., Stroomberg, G. J., Van der Molen, A. J. & Prokop, M. Review of strategies to reduce the contamination of the water environment by gadolinium-based contrast agents. *Insights Imaging* **15**, 62 (2024). <https://doi.org/10.1186/s13244-024-01626-7>
- 6 Verplanck, P. L. *et al.* Evaluating the behavior of gadolinium and other rare earth elements through large metropolitan sewage treatment plants. *Environ Sci Technol* **44**, 3876-3882 (2010). <https://doi.org/10.1021/es903888t>
- 7 Klaver, G., Verheul, M., Bakker, I., Petelet-Giraud, E. & Négrel, P. Anthropogenic Rare Earth Element in rivers: Gadolinium and lanthanum. Partitioning between the dissolved and particulate phases in the Rhine River and spatial propagation through the Rhine-Meuse Delta (the Netherlands). *Applied Geochemistry* **47**, 186-197 (2014). <https://doi.org/https://doi.org/10.1016/j.apgeochem.2014.05.020>
- 8 Laczovics, A. *et al.* Relationship between gadolinium-based MRI contrast agent consumption and anthropogenic gadolinium in the influent of a wastewater treatment plant. *Sci Total Environ* **877**, 162844 (2023). <https://doi.org/10.1016/j.scitotenv.2023.162844>
- 9 Rabiet, M., Brissaud, F., Seidel, J. L., Pistre, S. & Elbaz-Poulichet, F. Positive gadolinium anomalies in wastewater treatment plant effluents and aquatic environment in the Hérault watershed (South France). *Chemosphere* **75**, 1057-1064 (2009). <https://doi.org/10.1016/j.chemosphere.2009.01.036>
- 10 Schmidt, K., Bau, M., Merschel, G. & Tepe, N. Anthropogenic gadolinium in tap water and in tap water-based beverages from fast-food franchises in six major cities in Germany. *Science of The Total Environment* **687**, 1401-1408 (2019). <https://doi.org/https://doi.org/10.1016/j.scitotenv.2019.07.075>

- 11 Ruffle, J., K., Mohinta, S., Gray, R., Hyare, H. & Nachev, P. Brain tumour segmentation with incomplete imaging data. *Brain Commun* **5** (2023). <https://doi.org/10.1093/braincomms/fcad118>
- 12 Gong, E., Pauly, J. M., Wintermark, M. & Zaharchuk, G. Deep learning enables reduced gadolinium dose for contrast-enhanced brain MRI. *J Magn Reson Imaging* **48**, 330-340 (2018). <https://doi.org/10.1002/jmri.25970>
- 13 Luo, H. *et al.* Deep learning-based methods may minimize GBCA dosage in brain MRI. *Eur Radiol* **31**, 6419-6428 (2021). <https://doi.org/10.1007/s00330-021-07848-3>
- 14 Ahmadzade, M., Morón, F. E., Shastri, R., M. Lincoln, C. & Rad, M. G. AI-Assisted Post Contrast Brain MRI: Eighty Percent Reduction in Contrast Dose. *Academic Radiology* (2024). <https://doi.org/https://doi.org/10.1016/j.acra.2024.10.026>
- 15 Muller-Franzes, G. *et al.* Using Machine Learning to Reduce the Need for Contrast Agents in Breast MRI through Synthetic Images. *Radiology* **307**, e222211 (2023). <https://doi.org/10.1148/radiol.222211>
- 16 Calabrese, E., Rudie, J. D., Rauschecker, A. M., Villanueva-Meyer, J. E. & Cha, S. Feasibility of Simulated Postcontrast MRI of Glioblastomas and Lower-Grade Gliomas by Using Three-dimensional Fully Convolutional Neural Networks. *Radiol Artif Intell* **3**, e200276 (2021). <https://doi.org/10.1148/ryai.2021200276>
- 17 Li, Z. *et al.* Deep learning-based non-contrast MRI model for nasopharyngeal carcinoma diagnosis: an end-to-end gadolinium-free solution. *npj Digital Medicine* **8**, 786 (2025). <https://doi.org/10.1038/s41746-025-02247-0>
- 18 Isensee, F., Jaeger, P. F., Full, P. M., Vollmuth, P. & Maier-Hein, K. in *BrainLes@MICCAI*.
- 19 Isensee, F., Jaeger, P. F., Kohl, S. A. A., Petersen, J. & Maier-Hein, K. H. nnU-Net: a self-configuring method for deep learning-based biomedical image segmentation. *Nat Methods* **18**, 203-211 (2021). <https://doi.org/10.1038/s41592-020-01008-z>
- 20 Myronenko, A. 3D MRI brain tumor segmentation using autoencoder regularization. arXiv:1810.11654 (2018). <https://ui.adsabs.harvard.edu/abs/2018arXiv181011654M>.
- 21 Hatamizadeh, A. *et al.* Swin UNETR: Swin Transformers for Semantic Segmentation of Brain Tumors in MRI Images. arXiv:2201.01266 (2022). <https://ui.adsabs.harvard.edu/abs/2022arXiv220101266H>.
- 22 Hatamizadeh, A. *et al.* UNETR: Transformers for 3D Medical Image Segmentation. *arXiv* (2021).
- 23 Isensee, F. *et al.* nnU-Net Revisited: A Call for Rigorous Validation in 3D Medical Image Segmentation. *arXiv e-prints*, arXiv:2404.09556 (2024). <https://doi.org/10.48550/arXiv.2404.09556>
- 24 Ruffle, J. K. *et al.* Computational limits to the legibility of the imaged human brain. *NeuroImage*, 120600 (2024). <https://doi.org/https://doi.org/10.1016/j.neuroimage.2024.120600>

- 25 Abramoff, M. D. *et al.* Considerations for addressing bias in artificial intelligence for health equity. *NPJ Digit Med* **6**, 170 (2023). <https://doi.org/10.1038/s41746-023-00913-9>
- 26 Carruthers, R. *et al.* Representational ethical model calibration. *NPJ Digit Med* **5**, 170 (2022). <https://doi.org/10.1038/s41746-022-00716-4>
- 27 Collins, G. S. *et al.* Protocol for development of a reporting guideline (TRIPOD-AI) and risk of bias tool (PROBAST-AI) for diagnostic and prognostic prediction model studies based on artificial intelligence. *BMJ Open* **11**, e048008 (2021). <https://doi.org/10.1136/bmjopen-2020-048008>
- 28 Bakas, S. *et al.* The University of Pennsylvania glioblastoma (UPenn-GBM) cohort: advanced MRI, clinical, genomics, & radiomics. *Scientific Data* **9**, 453 (2022). <https://doi.org/10.1038/s41597-022-01560-7>
- 29 Calabrese, E. *et al.* The University of California San Francisco Preoperative Diffuse Glioma MRI Dataset. *Radiol Artif Intell* **4**, e220058 (2022). <https://doi.org/10.1148/ryai.220058>
- 30 Baid, U. *et al.* The RSNA-ASNR-MICCAI BraTS 2021 Benchmark on Brain Tumor Segmentation and Radiogenomic Classification. (2021).
- 31 van der Voort, S. R. *et al.* The Erasmus Glioma Database (EGD): Structural MRI scans, WHO 2016 subtypes, and segmentations of 774 patients with glioma. *Data Brief* **37**, 107191 (2021). <https://doi.org/10.1016/j.dib.2021.107191>
- 32 Correia de Verdier, M. *et al.* The 2024 Brain Tumor Segmentation (BraTS) Challenge: Glioma Segmentation on Post-treatment MRI. *arXiv e-prints*, arXiv:2405.18368 (2024). <https://doi.org/10.48550/arXiv.2405.18368>
- 33 Moawad, A. W. *et al.* The Brain Tumor Segmentation - Metastases (BraTS-METS) Challenge 2023: Brain Metastasis Segmentation on Pre-treatment MRI. *ArXiv* (2024).
- 34 Fathi Kazerooni, A. *et al.* BraTS-PEDs: Results of the Multi-Consortium International Pediatric Brain Tumor Segmentation Challenge 2023. *arXiv e-prints*, arXiv:2407.08855 (2024). <https://doi.org/10.48550/arXiv.2407.08855>
- 35 LaBella, D. *et al.* A multi-institutional meningioma MRI dataset for automated multi-sequence image segmentation. *Sci Data* **11**, 496 (2024). <https://doi.org/10.1038/s41597-024-03350-9>
- 36 Adewole, M. *et al.* The Brain Tumor Segmentation (BraTS) Challenge 2023: Glioma Segmentation in Sub-Saharan Africa Patient Population (BraTS-Africa). *ArXiv* (2023).
- 37 Hunter, J. D. Matplotlib: A 2D Graphics Environment. *Computing in Science & Engineering* **9**, 90-95 (2007). <https://doi.org/10.1109/MCSE.2007.55>
- 38 The-MONAI-Consortium. Project MONAI. *Zenodo* (2020). <https://doi.org/https://doi.org/10.5281/zenodo.4323059>
- 39 Brett, Matthew, Markiewicz & Hanke, C. nipy/nibabel: 3.2.1 (Version 3.2.1). *Zenodo* (2020). <https://doi.org/http://doi.org/10.5281/zenodo.4295521>
- 40 Nilearn-contributors. *nilearn*, <<https://github.com/nilearn/nilearn>> (2024).

- 41 Harris, C. R. *et al.* Array programming with NumPy. *Nature* **585**, 357-362 (2020). <https://doi.org/10.1038/s41586-020-2649-2>
- 42 Reback, J., McKinney, W. & jbrockmendel. pandas-dev/pandas: Pandas 1.0.3 (Version v1.0.3). *Zenodo* (2020). <https://doi.org/http://doi.org/10.5281/zenodo.3715232>
- 43 Paszke, A. *et al.* PyTorch: An Imperative Style, High-Performance Deep Learning Library. *NeurIPS* (2019).
- 44 Waskom, M. & Seaborn-Development-Team. seaborn. *Zenodo* (2020). <https://doi.org/https://doi.org/10.5281/zenodo.4645478>
- 45 Pedregosa, F., Varoquaux, G. & Gramfort, A. Scikit-learn: Machine Learning in Python. *Journal of Machine Learning Research* **12**, 2825-2830 (2011). <https://doi.org/10.48550/arXiv.1201.0490>
- 46 Kleesiek, J. *et al.* Can Virtual Contrast Enhancement in Brain MRI Replace Gadolinium?: A Feasibility Study. *Invest Radiol* **54**, 653-660 (2019). <https://doi.org/10.1097/RLI.0000000000000583>
- 47 Kono, K. *et al.* The role of diffusion-weighted imaging in patients with brain tumors. *AJNR Am J Neuroradiol* **22**, 1081-1088 (2001).
- 48 Ammari, S. *et al.* Can Deep Learning Replace Gadolinium in Neuro-Oncology?: A Reader Study. *Invest Radiol* **57**, 99-107 (2022). <https://doi.org/10.1097/RLI.0000000000000811>
- 49 Pasumarthi, S. *et al.* A generic deep learning model for reduced gadolinium dose in contrast-enhanced brain MRI. *Magn Reson Med* **86**, 1687-1700 (2021). <https://doi.org/10.1002/mrm.28808>
- 50 Murugesan, G. *et al.* Synthesizing Contrast-Enhanced MR Images from Noncontrast MR Images Using Deep Learning. *AJNR Am J Neuroradiol* **45**, 312-319 (2024). <https://doi.org/10.3174/ajnr.A8107>
- 51 Aggarwal, R. *et al.* Diagnostic accuracy of deep learning in medical imaging: a systematic review and meta-analysis. *NPJ Digit Med* **4**, 65 (2021). <https://doi.org/10.1038/s41746-021-00438-z>
- 52 Wenderott, K., Krups, J., Zaruchas, F. & Weigl, M. Effects of artificial intelligence implementation on efficiency in medical imaging—a systematic literature review and meta-analysis. *npj Digital Medicine* **7**, 265 (2024). <https://doi.org/10.1038/s41746-024-01248-9>
- 53 Guo, B. *et al.* The Impact of Scanner Domain Shift on Deep Learning Performance in Medical Imaging: an Experimental Study. *arXiv e-prints*, arXiv:2409.04368 (2024). <https://doi.org/10.48550/arXiv.2409.04368>
- 54 Dorfner, F. J., Patel, J. B., Kalpathy-Cramer, J., Gerstner, E. R. & Bridge, C. P. A review of deep learning for brain tumor analysis in MRI. *npj Precision Oncology* **9**, 2 (2025). <https://doi.org/10.1038/s41698-024-00789-2>

- 55 Dombrowski, M., Prenner, A. & Kainz, B. Bias Assessment and Data Drift Detection in Medical Image Analysis: A Survey. *arXiv e-prints*, arXiv:2409.17800 (2024). <https://doi.org/10.48550/arXiv.2409.17800>
- 56 Pati, S. *et al.* Federated learning enables big data for rare cancer boundary detection. *Nat Commun* **13**, 7346 (2022). <https://doi.org/10.1038/s41467-022-33407-5>
- 57 Wamelink, I. *et al.* Brain Tumor Imaging without Gadolinium-based Contrast Agents: Feasible or Fantasy? *Radiology* **310**, e230793 (2024). <https://doi.org/10.1148/radiol.230793>
- 58 Venugopal, V. K., Kumar, A., Tan, M. O. & Szarf, G. Curriculum check, 2025—equipping radiology residents for AI challenges of tomorrow. *Abdominal Radiology* (2025). <https://doi.org/10.1007/s00261-025-05016-5>

# **Predicting brain tumour enhancement from non-contrast MR imaging with artificial intelligence**

---

## **Supplementary Material**

## Materials and Methods

---

### Data

#### *Local data*

We included 3905 imaging sessions from 1364 unique patients who were imaged and treated for a glioma at our centre, the National Hospital for Neurology and Neurosurgery (NHNN), between 2006 and 2020, drawn from prospective histopathology record-keeping within the Institute's Department of Neuropathology. Having delineated a viable neuropathology cohort<sup>1</sup>, we retrieved all magnetic resonance imaging (MRI) scans from the Picture Archiving and Communications System (PACS). We also recorded diagnostic and demographic data in these individuals.

#### *External data*

We acquired multiple open-source datasets to boost sample sizes and maximise the generalizability of results in neuro-oncology internationally. The datasets and sample sizes used were as follows: 1) The Brain Tumour Segmentation Challenge (BraTS) (n=1470)<sup>2</sup>; 2) the Erasmus Glioma Dataset (EGD) (n=774)<sup>3</sup>; 3) The University of Pennsylvania Glioblastoma (UPenn-GBM) cohort (n=665)<sup>4</sup>; 4) The University of California San Francisco Preoperative Diffuse Glioma (UCSF-PDGM) cohort (n=501)<sup>5</sup>; 5) The Brain Tumour Segmentation – Post-treatment Challenge (n=1538)<sup>6</sup>; 6) The Brain Tumour Segmentation – Metastases Challenge (n=739)<sup>7</sup>; 7) The Brain Tumour Segmentation – Paediatric Challenge (n=352)<sup>8</sup>; 8) The Brain Tumour Segmentation – Meningioma Challenge (n=1000)<sup>9</sup>, and 9) The Brain Tumour Segmentation – Glioma in Sub-Saharan Africa Challenge (n=145)<sup>10</sup>. In instances of crossover between datasets (such as the inclusion of UCSF-PDGM<sup>5</sup> and UPenn-GBM<sup>4</sup>, which both feature, in part, in BraTS2021<sup>2</sup>), we contacted the principal investigators of each study to clarify those specific cases and ensure that no participants were erroneously duplicated in our set. As a secondary quality control measure, any lesion whose appearance was highly correlated (voxel-wise  $r > 0.95$ ) was flagged for cross-checking to ensure no duplicate participants. Paired demographics were variably available for these external repositories, the completeness of which was beyond our control.

### Image pre-processing

We acquired all available MRI sequences for all available imaging sessions from our local neuro-oncology cohort, with data ranging from 2006 to 2024. We deployed a locally developed MRI sequence classifier and artefact detector for initial image quality control and to curate imaging sequences<sup>11</sup>. We clamped MRI signal intensities at the 1<sup>st</sup> - 99<sup>th</sup> percentile to attenuate any spurious signal artefacts. All sequences were super-resolved to 1x1x1mm isotropic resolution using a locally developed generative super-resolution model<sup>12</sup>. Images were brain extracted with HD-BET<sup>13</sup>, from which the brain extraction masks were also curated. We manually reviewed all raw data at all stages of the data pre-processing.

#### *Ground truth enhancing tumour masks*

Ground truth-enhancing tumour masks were always generated from non-contrast T1-, T2-, T2/FLAIR-, and post-contrast T1-weighted imaging (i.e., complete datasets), which were available for all patients. For external datasets, this was already available as described above. For local data, we deployed an in-house tumour segmentation model, applied to complete datasets where post-contrast imaging was available to derive labels for enhancing tumour,

non-enhancing tumour, and perilesional signal change, previously validated elsewhere and openly available online<sup>14</sup>. Inferred labels were reviewed before their downstream application by a neuroradiologist with 7 years of neuro-oncology experience.

#### *Nonlinear anatomical registration with enantiomorphic normalisation*

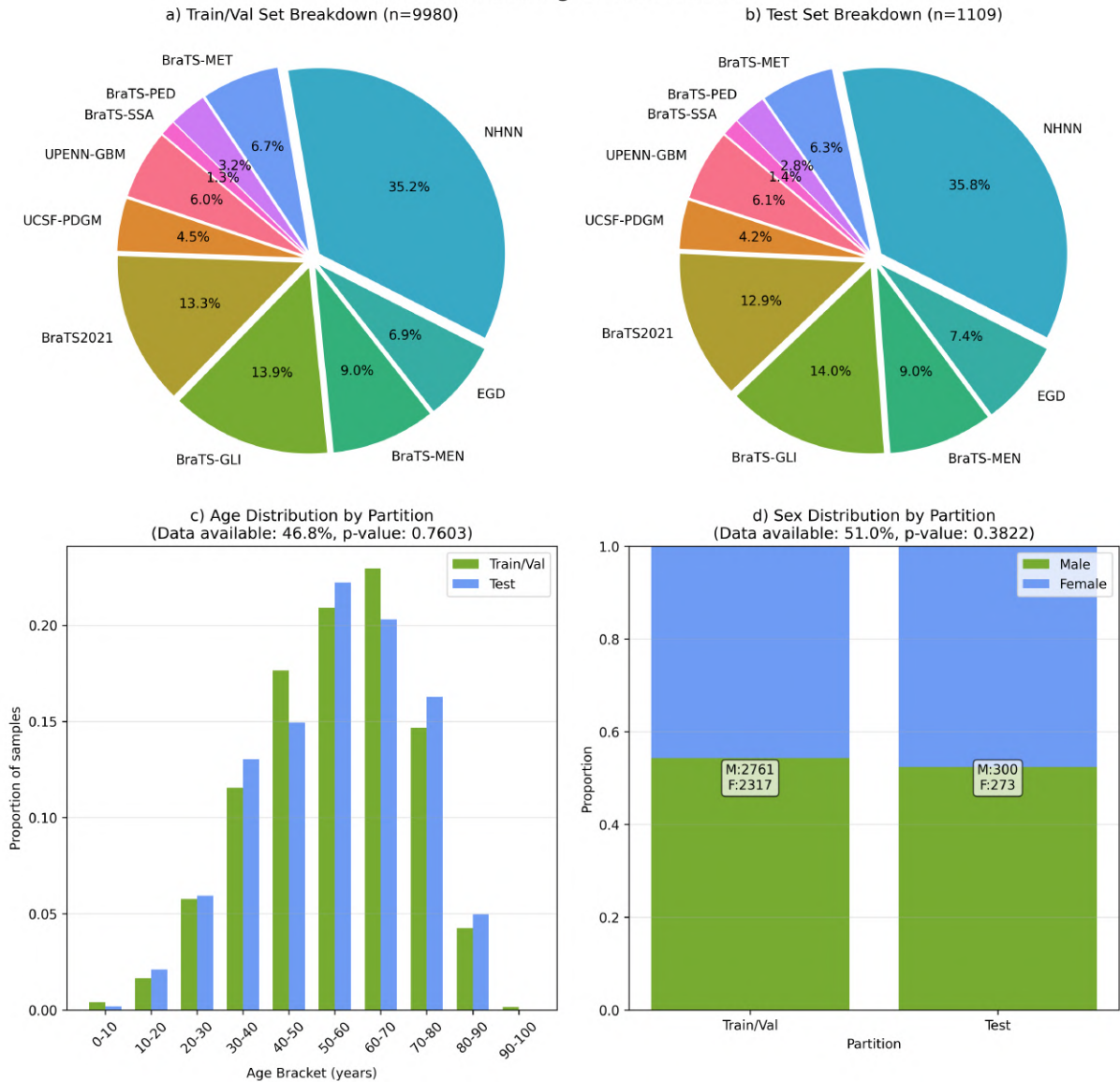
Having segmented lesions in the patient's native space, structural and lesion segmentation masks were nonlinearly registered to 1x1x1mm isotropic resolution MNI space with Statistical Parametric Mapping (SPM, v12) and enantiomorphic correction<sup>15,16</sup>. The advantage of enantiomorphic correction is that the risks of registration errors secondary to a lesion are minimised by leveraging a given patient's normal structural neuroanatomy on the unaffected contralesional hemisphere<sup>15</sup>.

## **Evaluation**

### *Equity calibration*

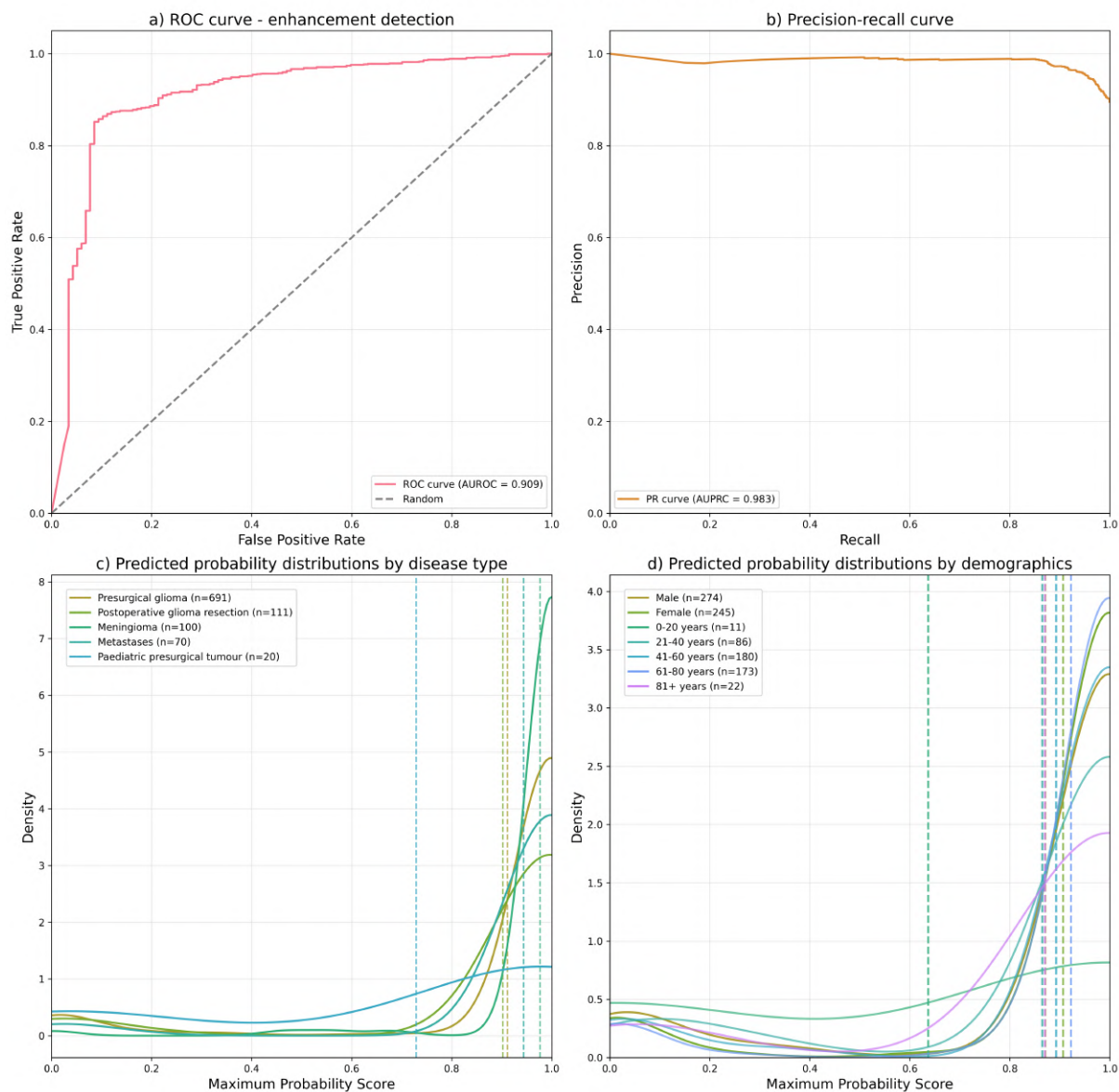
This process was supported by Fairboard, a novel digital platform for equitable model calibration. We also quantified the model detection rate in relation to radiomic features of enhancement, determining the relationship between segmentation performance and whether it was infiltrative, irregular/complex, well-circumscribed, solitary or multiple. The radiomic categories were defined based on quantitative shape features extracted from 3D binary masks of enhancing brain lesions. The following features were calculated: 1) Number of connected components from 3D connected component analysis; 2) Sphericity, calculated as  $\frac{\pi^{\frac{1}{3}}(6V)^{\frac{2}{3}}}{A}$ , where  $V$  denotes volume and  $A$  is surface area; 3) Solidity: calculated as the ratio of actual lesion volume to convex hull volume; 4) Compactness, calculated as  $\frac{A^3}{(36\pi V^2)}$ , where  $A$  is surface area and  $V$  is volume; 5) Surface-to-Volume Ratio, the surface area divided by volume; and 6) Elongation, ratio of largest to smallest eigenvalues from principal component analysis of lesion voxel coordinates. Based on these quantitative features, lesions were classified into the following radiomic categories: 1) Multiple – imaging sessions with  $\geq 3$  connected components, or two components where the largest component represents  $< 80\%$  of total enhancement volume; 2) Well-circumscribed single - a single dominant lesion with sphericity  $> 0.7$  and solidity  $> 0.9$ ; 3) Infiltrative single - a single dominant lesion with sphericity  $< 0.5$  or solidity  $< 0.7$ ; 4) Irregular/complex single – a single dominant lesion with intermediate features of sphericity  $0.5 - 0.7$  and solidity  $0.7 - 0.9$ .

## Data Partitioning Characteristics



**Supplementary Figure 1. Data partitioning characteristics.** a) Training and validation set composition (n=9,980) showing proportional representation across all cohorts. b) Test set composition (n=1,109), maintaining equivalent proportions to training data, ensuring unbiased evaluation. c) Age distribution comparison between training/validation and test set partitions. d) Sex distribution comparison between training/validation and test set partitions.

Model discriminative performance analysis



**Supplementary Figure 2. Model discriminative performance analysis.** a) Receiver Operating Characteristic (ROC) and b) Precision-Recall curve for enhancement detection. c) Predicted probability distributions stratified by pathology type and d) demographics.

## References

- 1 Ruffle, J. K. *et al.* Brain tumour genetic network signatures of survival. *Brain* **146**, 4736–4754 (2023). <https://doi.org/https://doi.org/10.1093/brain/awad199>
- 2 Baid, U. *et al.* *The RSNA-ASNR-MICCAI BraTS 2021 Benchmark on Brain Tumor Segmentation and Radiogenomic Classification.* (2021).
- 3 van der Voort, S. R. *et al.* The Erasmus Glioma Database (EGD): Structural MRI scans, WHO 2016 subtypes, and segmentations of 774 patients with glioma. *Data Brief* **37**, 107191 (2021). <https://doi.org/10.1016/j.dib.2021.107191>
- 4 Bakas, S. *et al.* The University of Pennsylvania glioblastoma (UPenn-GBM) cohort: advanced MRI, clinical, genomics, & radiomics. *Scientific Data* **9**, 453 (2022). <https://doi.org/10.1038/s41597-022-01560-7>
- 5 Calabrese, E. *et al.* The University of California San Francisco Preoperative Diffuse Glioma MRI Dataset. *Radiol Artif Intell* **4**, e220058 (2022). <https://doi.org/10.1148/ryai.220058>
- 6 Correia de Verdier, M. *et al.* The 2024 Brain Tumor Segmentation (BraTS) Challenge: Glioma Segmentation on Post-treatment MRI. *arXiv e-prints*, arXiv:2405.18368 (2024). <https://doi.org/10.48550/arXiv.2405.18368>
- 7 Moawad, A. W. *et al.* The Brain Tumor Segmentation - Metastases (BraTS-METS) Challenge 2023: Brain Metastasis Segmentation on Pre-treatment MRI. *ArXiv* (2024).
- 8 Fathi Kazerooni, A. *et al.* BraTS-PEDs: Results of the Multi-Consortium International Pediatric Brain Tumor Segmentation Challenge 2023. *arXiv e-prints*, arXiv:2407.08855 (2024). <https://doi.org/10.48550/arXiv.2407.08855>
- 9 LaBella, D. *et al.* A multi-institutional meningioma MRI dataset for automated multi-sequence image segmentation. *Sci Data* **11**, 496 (2024). <https://doi.org/10.1038/s41597-024-03350-9>
- 10 Adewole, M. *et al.* The Brain Tumor Segmentation (BraTS) Challenge 2023: Glioma Segmentation in Sub-Saharan Africa Patient Population (BraTS-Africa). *ArXiv* (2023).
- 11 Kanber, B., Ruffle, J., Cardoso, J., Ourselin, S. & Ciccarelli, O. Neurosense: deep sensing of full or near-full coverage head/brain scans in human magnetic resonance imaging. *Neuroinformatics* **18**, 333-336 (2020). <https://doi.org/10.1007/s12021-019-09442-x>
- 12 Brudfors, M., Balbastre, Y., Nachev, P. & Ashburner, J. MRI Super-Resolution Using Multi-channel Total Variation. *Medical Image Understanding and Analysis*, 217-228 (2018). [https://doi.org/https://doi.org/10.1007/978-3-319-95921-4\\_21](https://doi.org/https://doi.org/10.1007/978-3-319-95921-4_21)
- 13 Isensee, F. *et al.* Automated brain extraction of multisequence MRI using artificial neural networks. *Human Brain Mapping* **40**, 4952-4964 (2019). <https://doi.org/https://doi.org/10.1002/hbm.24750>

- 14 Ruffle, J., K., Mohinta, S., Gray, R., Hyare, H. & Nachev, P. Brain tumour segmentation with incomplete imaging data. *Brain Commun* **5** (2023). <https://doi.org/10.1093/braincomms/fcad118>
- 15 Nachev, P., Coulthard, E., Jager, H. R., Kennard, C. & Husain, M. Enantiomorphic normalization of focally lesioned brains. *Neuroimage* **39**, 1215-1226 (2008). <https://doi.org/10.1016/j.neuroimage.2007.10.002>
- 16 Ashburner, J. & Friston, K. J. Nonlinear spatial normalization using basis functions. *Hum Brain Mapp* **7**, 254-266 (1999). [https://doi.org/10.1002/\(SICI\)1097-0193\(1999\)7:4<#x0003c;254::AID-HBM4>#x0003e;3.0.CO;2-G](https://doi.org/10.1002/(SICI)1097-0193(1999)7:4<#x0003c;254::AID-HBM4>#x0003e;3.0.CO;2-G)